



Article

Optimization of Process Conditions for Additive Manufacturing Technology Combining High-Power Diode Laser and Hot Wire [†]

Song Zhu * , You Nakahara and Motomichi Yamamoto * 

Graduate School of Engineering, Hiroshima University, Higashi-Hiroshima 739-0046, Japan; m206583@hiroshima-u.ac.jp

* Correspondence: d192020@hiroshima-u.ac.jp (S.Z.); motoyama@hiroshima-u.ac.jp (M.Y.); Tel.: +81-70-1260-2026 (S.Z.); +81-82-424-7815 (M.Y.)

[†] Presented at the 1st International Electronic Conference on Metallurgy and Metals; 22 February–7 March 2021.

Abstract: A high-efficiency additive manufacturing technology that combines a high-power diode laser with a large-rectangle spot (beam width of 11 mm) and a hot-wire system was developed. The hot-wire system can generate Joule heat by wire current and heat a filler to its melting point independently from the main heat source of a high-power diode laser. A simple calculation method to derive the appropriate hot-wire current of Z3321-YS308L was proposed with verification by hot-wire feeding experiments without laser irradiation at various wire currents. The effect of process parameters, such as laser power, process speed, and the wire feeding rate (wire feeding speed/process speed) on bead characteristics was investigated by cross-sectional evaluations on three-layer depositions. High-speed imaging observations of wire melting and molten pool formation showed that the energy density input and the wire feeding rate were dominant parameters in terms of bead formation and hot-wire feeding stability. A 50-mm-high, 8-mm-wide, and 250-mm-long sample was fabricated by using appropriate process conditions, and tensile tests were performed by using a sub-sample from the large sample.

Keywords: additive manufacturing; diode laser; hot wire; high efficiency; high material utilization



Citation: Zhu, S.; Nakahara, Y.; Yamamoto, M. Optimization of Process Conditions for Additive Manufacturing Technology Combining High-Power Diode Laser and Hot Wire. *Metals* **2021**, *11*, 1583. <https://doi.org/10.3390/met11101583>

Academic Editors: Eric D. van Hullebusch and Golden Kumar

Received: 1 September 2021

Accepted: 3 October 2021

Published: 4 October 2021

Publisher's Note: MDPI stays neutral with regard to jurisdictional claims in published maps and institutional affiliations.



Copyright: © 2021 by the authors. Licensee MDPI, Basel, Switzerland. This article is an open access article distributed under the terms and conditions of the Creative Commons Attribution (CC BY) license (<https://creativecommons.org/licenses/by/4.0/>).

1. Introduction

Research, development, and practical application of additive manufacturing (AM) technologies, such as three-dimensional (3D) printing processes, have been carried out actively over recent years [1–3]. Compared with traditional subtractive manufacturing methodologies, AM technology yields continuous material accumulation by layer-by-layer addition and high-accuracy and complex 3D components through computer-controlled technology [4–6]. Because of these characteristics, AM technology has received extensive attention and has been applied in various industrial fields [7–10].

State-of-the-art studies have shown that metal-based AM technology can be categorized into three types according to the heat source: wire and arc additive manufacturing (WAAM), electron beam freeform fabrication (EBF³), and laser additive manufacturing (LAM) [11,12]. Although wire and arc additive manufacturing has the advantages of a high fabrication efficiency, low equipment cost, large component manufacturing capability, and defect-forming prevention compared with other AM technologies, it has challenges, such as control of heat input, low cooling rates, large distortion, and surface fouling [13–18]. To reduce the heat input, ultracold-wire arc AM and hot wire WAAM have been proposed by Rodrigues et al. and Li et al. [19,20]. Development of the EBF³ method has been accelerated because of its ability to manufacture high-quality near-net-shape components with better mechanical properties and little material waste by using an electron beam as a heat source in a vacuum chamber. This method also has problems, such as a low deposition

rate, the requirement for a vacuum environment, and a high equipment price [12,21,22]. The LAM method has been applied widely and uses a high-energy density laser that is irradiated on a substrate or previous layer using metallic powders as common additive materials. Two powder material feeding processes are used: the powder-bed-fusion (PBF) type and the metal-deposition type. PBF provides small-size (40~100 μm) parts with a low laser power (<500 W), high precision, and flexibility. However, the LAM method that uses powder materials also has disadvantages, such as a low deposition rate, high material cost, and defect formations [23–25]. The use of wire materials can improve the deposition rate significantly compared with the use of powder materials with a lower utilization rate (20%) [26,27]. However, the conventional LAM process that uses cold wire materials remains an ongoing challenge because of the high reflectivity on some materials, the inability to control base metal melting and cold wire melting independently, and small process condition tolerances [28,29]. Therefore, the LAM method combined with a hot-wire system is interesting because of its high productivity and controllability.

Hot-wire laser additive manufacturing (HLAM) is a promising and potential manufacturing method because of its high deposition efficiency at a low laser power that results from its dual heat sources. A laser beam with a high controllability serves as the main heat source, and another heat source is Joule heat that is generated by a wire current, which heats the filler wire to its melting point independently from the heat input of the main heat source for base metal melting. The advantages of the HLAM method compared with the cold-wire LAM method are a higher productivity without an increase in heat input, a high freedom in material choice, and a high material utilization [30,31]. Wen et al. [32] proposed that a laser process with a preheating of the filler wire to an appropriate temperature could improve the welding efficiency and deposition rate significantly and reduce the heat input. Shinozaki et al. [33] clarified that wire tip melting was affected mainly by the wire current, the feeding position, and the feeding angle. These process conditions need to be controlled within suitable ranges. The filler wire temperature is the main parameter that is required to maintain wire melting phenomena. In the layer-upon-layer process, an unsuitable wire temperature results in spatter generation and a non-uniform deposited layer with defects. Liu et al. [34] found that the laser process with a hot wire reduced the laser power consumption and heat input. Nurminen et al. [35] compared laser processes using powder, cold-wire, and hot-wire feeding and found that the laser process with the hot wire reduced the dilution rate and increased the deposition rate. The hot-wire process improved the deposition efficiency two to four times compared with the powder and cold-wire processes. Wei et al. [36] found that the laser process with hot-wire feeding improved the energy efficiency coefficient and reduced the energy consumption by ~16% compared with the cold-wire process.

The novel hot-wire laser process with a high-power diode laser has been investigated and developed [37–39]. The diode laser has advantages of beam shape flexibility, a large beam creation (beam width over 10 mm), and a highly controllable and uniform energy distribution (1 mm \times 12 mm rectangular spot) in a large beam spot compared with the fiber laser (0.4–1 mm circular spot) [40]. The HLAM combined with a high-power diode laser has a large potential to produce a large, wide, and flexible-sized product with a high productivity, a high material utilization, and a low heat input.

In this study, the appropriate process conditions for JIS-Z3321-YS308L filler wire were investigated by HLAM using a high-power diode laser as a main heat source with a large rectangular beam spot. A simple calculation method to derive the hot-wire temperature distribution and the appropriate heating current was derived. Hot-wire feeding experiments without laser irradiation at various wire currents were performed to obtain appropriate heating currents. The effect of process parameters, such as laser power, process speed, and the wire feeding rate (wire feeding speed/process speed) on bead characteristics, such as the effective width, effective height, maximum height, and the near net shape rate, was investigated by cross-sectional evaluations on three-layer depositions. The phenomena and stabilities of bead formation and hot-wire feeding during multi-layer deposition were

investigated based on high-speed video images. A wall-type sample of 50 mm in height, 8 mm in width, and 250 mm in length was fabricated with a high efficiency and high material utilization using appropriate process conditions. Tensile tests were performed by using a tensile test specimen that was cut from the wall-type sample.

2. Materials and Methods

2.1. Materials

A JIS-Z3321-YS308L filler wire with a 1.2-mm-diameter and a base metal of 590-MPa-class steel plate with a 200-mm length, a 100-mm width, and a 9-mm thickness were used. The chemical compositions of the filler wire and base metal are shown in Table 1. Oxide on the base-metal surface was polished and degreased with acetone before the experiment.

Table 1. Chemical compositions of Z3321-YS308L and 590-MPa-class steel plate (wt.%).

Element	C	S	Mn	P	S	Ni	Cr	Mo	Fe
Wire	0.01	0.38	1.60	0.024	0.001	9.98	19.87	0.09	Bal.
BM	0.08	0.38	1.50	0.011	0.002	0.01	0.21	0.01	Bal.

2.2. Experimental Setup

Figure 1a shows a schematic diagram of the experimental setup of the HLAM process. Figure 1b shows the laser head created by the combination of fiber core diameters (0.4 mm), collimator lens (100 mm), homogenizer, and focusing lens (400 mm), which decided the rectangular beam width and length. The HLAM process used a 6-kW high-power diode laser with a large rectangle beam spot and a high-power wire heating power supply with a maximum current above 400 A. Six kW is high-power compared with the PBF process; however, the HLAM process uses the much larger laser spot size (1.6×11 mm)—in other words, the laser energy distribution of HLAM is relatively small. In addition, the deposition rate of HLAM is much larger than that of PBF. The high-power wire heating power supply can heat the filler wire to its melting point under the high-speed condition for filler wire feeding. A specimen was fixed on a biaxial slide table to achieve precise and stable motion. The filler wire was fed from the front as the wire leading process.

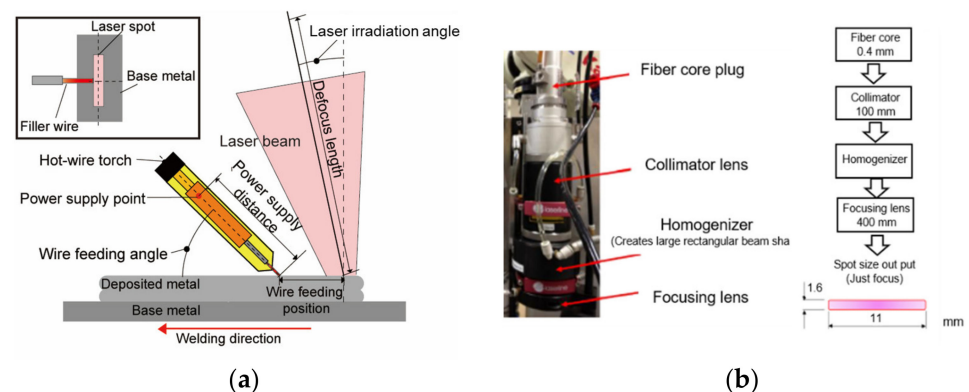


Figure 1. HLAM experimental setup: (a) schematic diagram of HLAM process; (b) laser head and beam shape.

Table 2 shows the process parameters that were used in the HLAM experiment. A wide (width of 11 mm) and narrow (length of 1.6 mm) rectangular beam spot was used, and the laser irradiation angle was fixed at 5° . The process parameters, such as laser power, process speed, wire current, and the wire feeding rate (wire feeding speed/process speed), were varied. Forward wire feeding and a 45° angle between the substrate and the filler wire were used. Argon gas (100%, 30 L/min) was used for shielding with a shielding box.

Table 2. Process parameters.

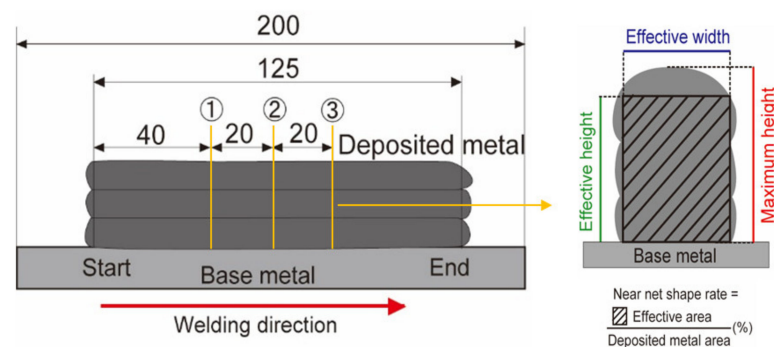
Content	Value
Laser power, kW	3.3~5.5
Laser irradiation angle, deg	5
Laser spot size, mm	$1.6^L \times 11^W$
Process speed, m/min	0.24~0.5
Wire feeding speed, m/min	5~20
Wire current, A	118~234
Power supply distance, mm	50
Wire feeding rate	20~40
Wire feeding angle, deg	45
Shielding gas (Ar), L/min	30
Welding direction	Forward

To clarify the deposition process, the phenomena of molten pool formation and filler wire melting during deposition were observed by high-speed camera imaging with imaging conditions listed in Table 3. Lighting laser illumination with a 808-nm wavelength was used to acquire bright images, and a bandpass filter with a transmitted wavelength of 810 ± 10 nm was installed with an optical lens.

Table 3. Imaging conditions.

Content	Value
Frame rate, fps	1000
Ban pass filter, nm/FWHM	810 ± 10
Laser lighting wavelength, nm	808
Laser lighting power, W	30
Shutter speed, s	1/5000

Figure 2 shows a schematic diagram of cross-sectional sampling locations, with ①, ②, and ③ indicating deposition starting points at 40, 60, and 80 mm, respectively. The polished cross-section was evaluated in terms of the effective width, the effective height, the maximum height, and the near net shape rate, as shown in Figure 2. Figure 3 shows a schematic illustration of the large wall-type sample and a cut-off plan for the tensile test specimen based on JIS Z2201 No.14-B.

**Figure 2.** Cross-sectional sampling locations and evaluated parameters (mm).

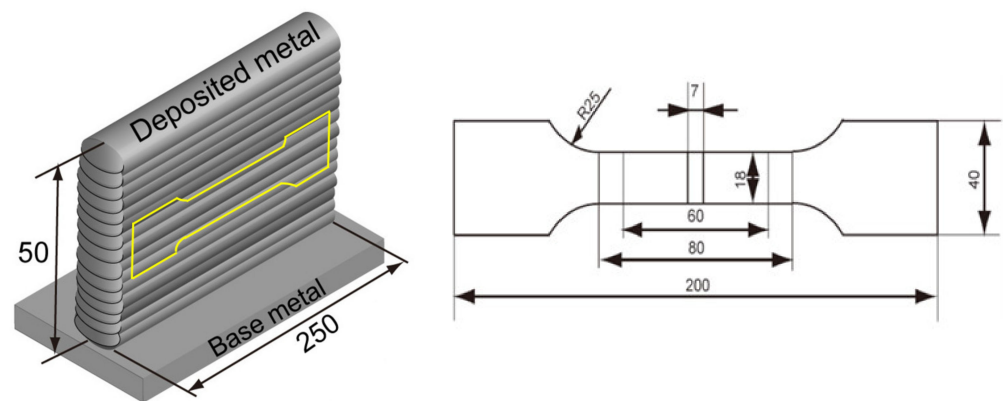


Figure 3. Large wall-type sample and cut-off plan for tensile test specimen (JIS Z2201 No.14-B).

2.3. Simple Calculation Method for Appropriate Hot-Wire Current

Figure 4 shows a simple calculation method to derive a hot-wire temperature distribution during feeding and an appropriate hot-wire current to heat the wire tip to its melting point at various wire feeding speeds. The proposed method divides the power supply distance (50 mm) into a small length of 0.1 mm (L) to obtain a precise temperature increase (ΔT) according to the temperature-dependent electric resistance. Joule heating by contact resistance at the power supply point was added to the electric resistance at the start point.

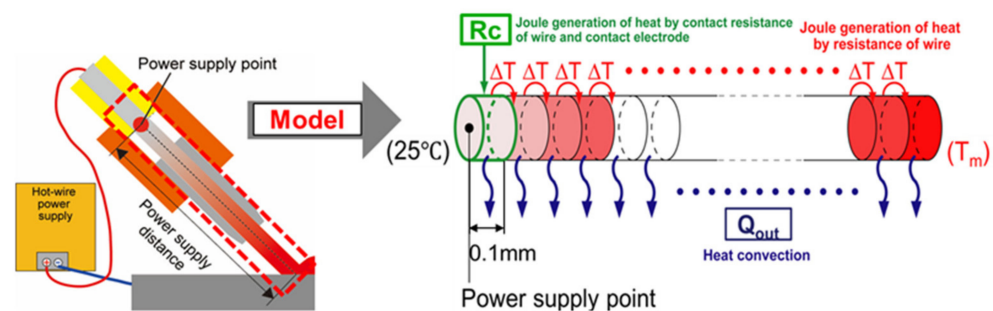


Figure 4. Schematic diagram of simple current calculation method for appropriate hot-wire current.

The calculation method is shown by Equations (1)–(3). Equation (1) shows the net heat increase Q in each divided region (0.1 mm) of the filler wire, which is equal to the heat input into the region (Q_{in}) minus the heat loss from the region.

$$Q = Q_{in} - Q_{out} \quad (1)$$

where

$$Q_{in} = I^2 \times R(T) \times t \quad (2)$$

$$Q_{out} = h \times A \times (T_w - T_R) \quad (3)$$

Q_{in} is the heat generated by the temperature-dependent electric resistance of the filler wire material at each divided region (0.1 mm), in J; Q_{out} is the heat loss from each divided region (0.1 mm) during wire feeding, in J; I is the hot-wire heating current, in A; $R(T)$ is the temperature-dependent electric resistance of the filler wire material, in Ω ; t is the heating time for each divided region (0.1 mm), in s; h is the comprehensive heat loss coefficient, in $W/m^2 \cdot K$; T_w is the wire temperature, in $^{\circ}C$; and T_R is room temperature, in $^{\circ}C$.

The electric resistance $R(T)$ at temperature T of the L (0.1 mm) segment of the filler wire is given as follows: multiplication

$$R(T) = \{\rho(T) + R_c\} \times L / \pi r^2 \quad (4)$$

where $\rho(T)$ is the temperature-dependent specific electrical resistivity, in $\Omega \cdot m$, and r is the radius of the filler wire, in mm. R_c is the contact resistance, in Ω .

The heating time (t) for heating through the region of length L (0.1 mm) is given as follows:

$$t = 60 \times L \times D / V_f \quad (5)$$

where D is the duty ratio of the wire heating current, and V_f is the wire feeding speed, in m/min. The temperature increase through the region of length L (ΔT) is given as follows:

$$\Delta T = Q / c(T) \times m(T) \times L \times \pi r^2 \quad (6)$$

where $c(T)$ is the temperature-dependent specific heat, in $J/kg \cdot ^\circ C$, and $m(T)$ is the temperature-dependent specific gravity, in kg/m^3 .

Equations (1)–(6) can be used to obtain the appropriate current for a wire tip temperature below the melting point at various wire feeding speeds before the multi-layer deposition experiment is performed.

2.4. Definitions of Energy Heat Input and Wire Feeding Rate

The process conditions, such as laser power, energy density of the laser beam, process speed, and wire feeding speed, affect the processing phenomena, the bead formation, and the deposited layer quality. The effect of combinations of these parameters, such as energy heat input and the wire feeding rate, on melting phenomena during processing should be considered. The definitions of the energy heat input (J/mm^3) and the wire feeding rate are provided in Equations (7) and (8).

$$\text{Energy heat input} = \frac{P}{A_s \times V_p} \quad (7)$$

$$\text{Wire feeding rate} = \frac{V_f}{V_p} \quad (8)$$

where P is the laser power, in W; A_s is the area of the laser spot size, in mm; V_p is the process speed, in m/min; and V_f is the wire feeding speed, in m/min.

3. Results

3.1. Comparison of Calculated and Experimental Appropriate Hot-Wire Currents

Figure 5 compares the calculated and experimental appropriate hot-wire current at various wire feeding speeds. When a contact resistance (R_c) of 0.004Ω and a comprehensive heat loss coefficient (h) of $1 W/m^2 \cdot K$ were used, the calculated hot-wire current of Z3321-YS308L wire at all wire feeding speeds agreed with the experimental current that was obtained when the wire feeding speeds varied from 5 to 20 m/min. The hot-wire current was estimated at various conditions (e.g., wire diameter, wire feeding speed) before being combined with laser irradiation for multi-layer deposition by using the proposed simple calculation method.

3.2. Bead Appearance Evaluation

Figure 6 shows typical bead appearances of three-layer depositions of sound beads and wire stubbing beads. After calculating the hot-wire current by the previous method, sound beads without defects were obtained by combining suitable process parameters (see Figure 6a). When the process parameters were unsuitable, for example, the wire feeding rate was greater than the constant combination of laser power and process speed, and a low-quality bead-like wire stubbing was observed (see Figure 6b).

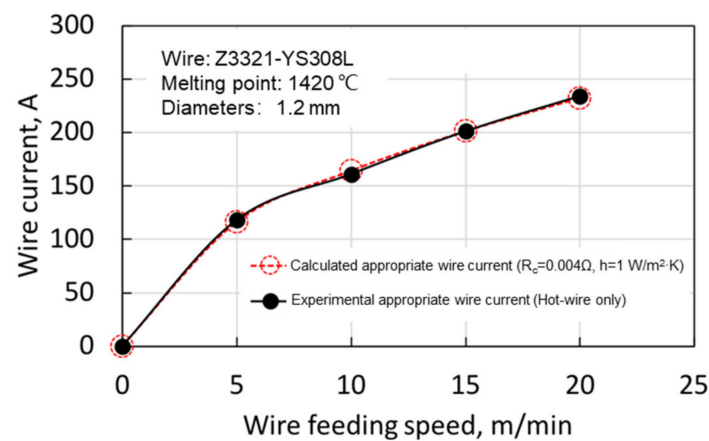


Figure 5. Comparison between calculated and experimental appropriate hot-wire current.



Figure 6. Typical bead appearances. (a) Sound bead and (b) wire stubbing.

Figure 7 shows the process windows of bead appearance evaluation under process parameter combinations of (a) laser power and process speed, and (b) laser power and the wire feeding rate. The red circles indicate the sound bead, and the black crosses indicate a bead with the typical defect of bead appearance. As shown in Figure 7a, when the wire feeding rate was fixed at 20, the lowest laser power limit existed for each process speed. As the process speed increased, a higher laser power was required to obtain the sound bead. The laser power should be combined with the appropriate process speed to achieve sufficient heat input for the sound and stable processing phenomena. When the process conditions were unsuitable, for example, the laser power was too low or the process speed was too high, and the inadequate lower heat input led to unstable processing phenomena and poor-quality beads. As shown in Figure 7b, when the process speed (V_p) was fixed at 0.3 m/min, each wire feeding rate of the filler materials had laser power limitations to obtain sound bead appearances. A high and wide range of wire feeding rates from 20 to 40 was achieved for a 6-kW laser power by using HLAM.

3.3. Cross-Sectional Characteristics Evaluation

Figure 8 shows the bead appearances and cross-sections when the wire feeding rate was varied at ~ 30 with fixed combinations of a 5.5-kW laser power and a process speed of 0.36 m/min. A smooth bead appearance and stable cross-sectional shape without defects resulted for various wire feeding rates.

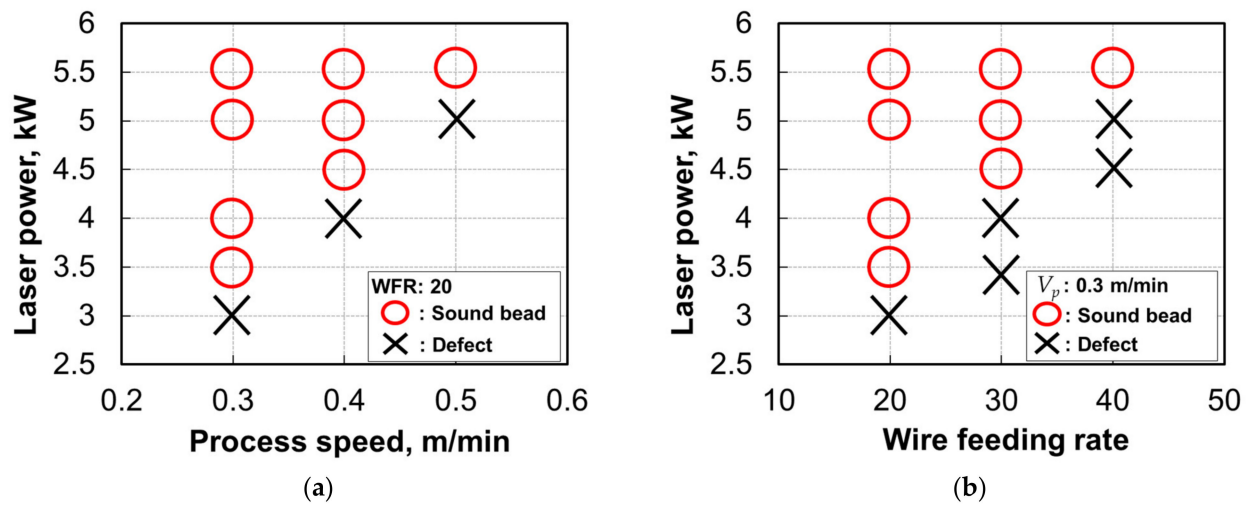


Figure 7. Process windows of bead appearance evaluation for process parameter combinations of (a) laser power and process speed and (b) laser power and the wire feeding rate.

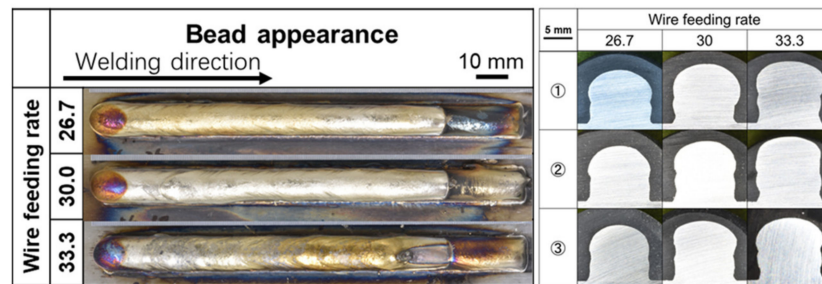


Figure 8. Bead appearances and cross sections for 5.5-kW laser power and a process speed of 0.36 m/min.

Figure 9 shows the cross-sectional characteristics at various wire feeding rates for a fixed laser power of 5.5 kW and a process speed of 0.36 m/min. An effective bead width of 10.2 mm with a laser spot width of 11 mm (see in Figure 9a), an effective height of 8.8 mm, a maximum height of 10.9 mm (see in Figure 9b), and a near net shape rate of 80% (see in Figure 9c) were obtained for a wire feeding rate of 33.3. The results prove that the proposed HLAM technology can create large parts with almost 100% material utilization and a high deposition rate of 814 cm³/h when a wire feeding rate of 33.3 and a process speed of 0.36 m/min are used.

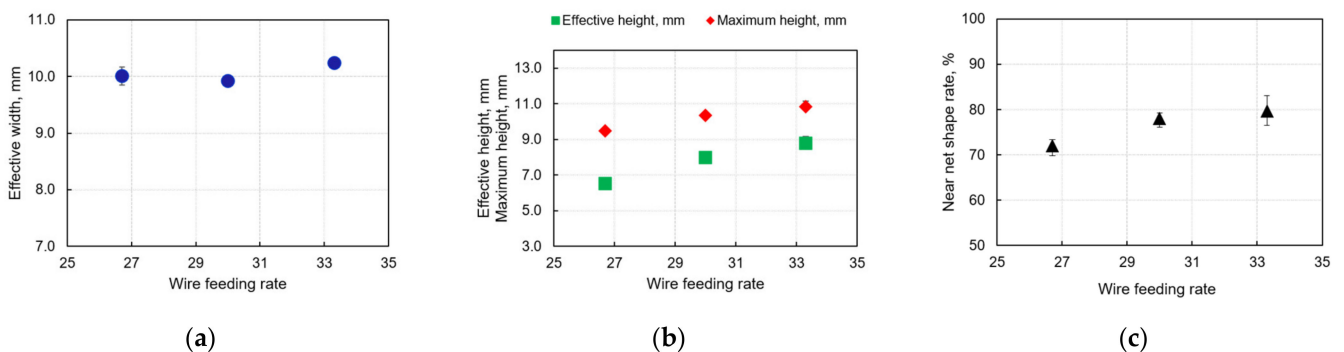


Figure 9. Cross-sectional characteristics of (a) effective width, (b) effective height and maximum height, and (c) near net shape rate, for laser power of 5.5 kW and process speed of 0.36 m/min.

3.4. Large Wall-Type Sample Manufacturing

Figure 10 shows the appearance and cross-section of the 15-layer wall-type sample that was fabricated by using the optimal process parameters from the above investigations, namely, a laser power of 5.5 kW, a process speed of 0.36 m/min, and a wire feeding rate of 33.3. A smooth and uniform appearance and a sound cross-section without any defects were obtained, although the fixed process parameters combined through all 15 layers. An effective height of 52.9 mm, a maximum height of 55.5 mm, an effective width of 8.8 mm, and a near net shape rate of 83% were obtained by using only 15 layers.

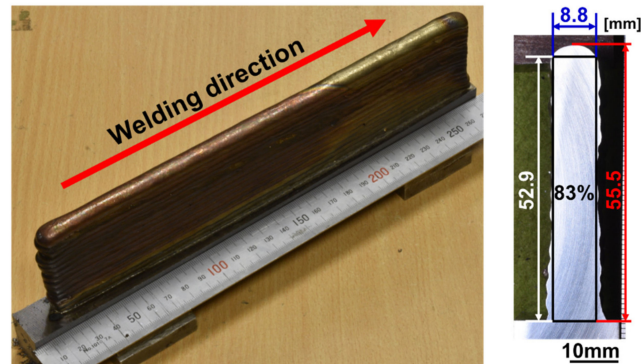


Figure 10. Appearance and cross-section of 15-layer large wall-type sample with measured values of effective height, maximum height, effective width, and near net shape rate.

Figure 11 shows the high-speed images that were captured on the first, fifth, tenth, and fifteenth layers during processing. The green, red, and yellow lines indicate the side shape of the molten pool, the hot-wire tip region, and the laser irradiating region, respectively. Stable molten pool formation and hot-wire feeding phenomena resulted, and almost the same phenomena were observed on all layers even when all process conditions were fixed from the first to the fifteenth layer on the substrate.

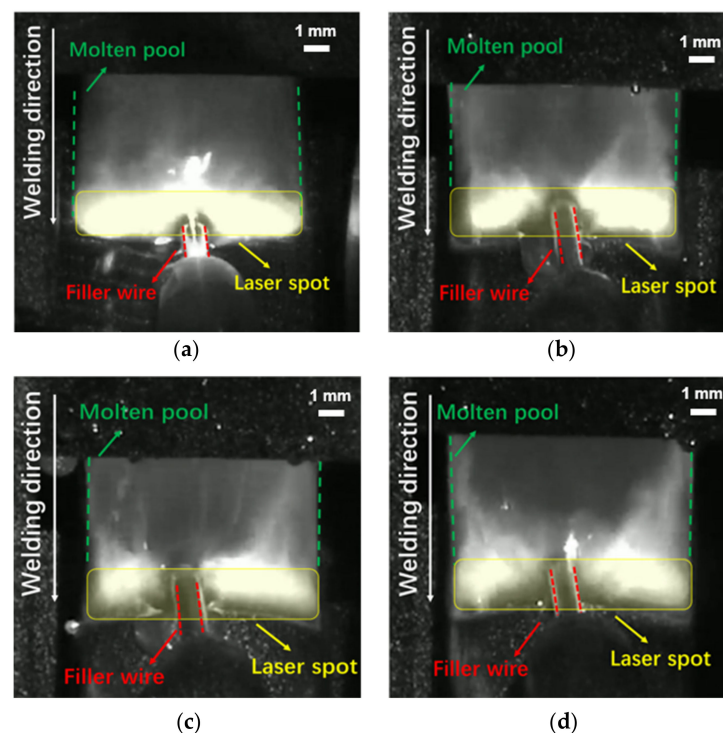


Figure 11. High-speed images on (a) first, (b) fifth, (c) tenth, and (d) fifteenth layer, during 15-layer deposition.

Figure 12 shows the load–displacement and stress–strain curves from the tensile tests using the specimen that was cut from the fabricated 15-layer wall-type sample, as shown in Figure 3. A tensile strength of 558 MPa and a 49% elongation were obtained. The tensile strength and elongation of the deposited metal meet the required values of the filler material. The above results indicate that the proposed HLAM process can achieve a stable process phenomena using a simple process parameter combination and sound-deposited sample with sufficient mechanical properties without any defects.

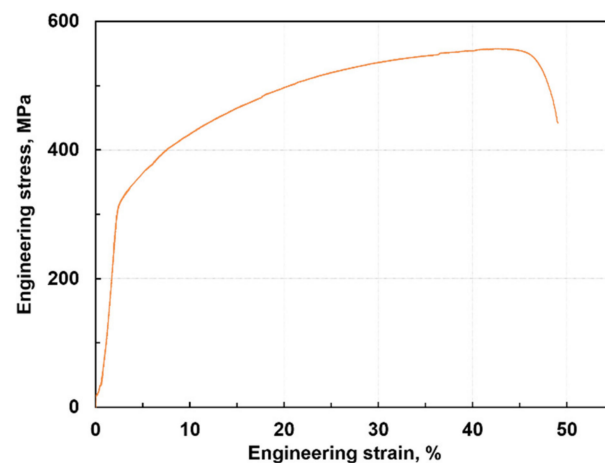


Figure 12. Load–displacement and stress–strain curves during tensile test.

4. Discussion

4.1. Effect of Hot-Wire Current on Wire Feeding Phenomena

Figure 13 shows high-speed images that indicate three typical types of hot-wire feeding phenomena without laser irradiation, sticking type, smooth feeding type, and fusing type. When the wire current was low, the hot-wire tip stuck on the substrate surface frequently, and unstable wire feeding occurred because insufficient wire heating could not increase the wire tip temperature (see Figure 13a). When the wire current was excessively high, fusing and spattering occurred because the hot-wire temperature reached its melting point before contacting the substrate (see Figure 13c). When the wire current was set to an appropriate value, the hot wire heated to its melting point at the wire tip on the substrate surface, and smooth and stable feeding was achieved (see Figure 13b).

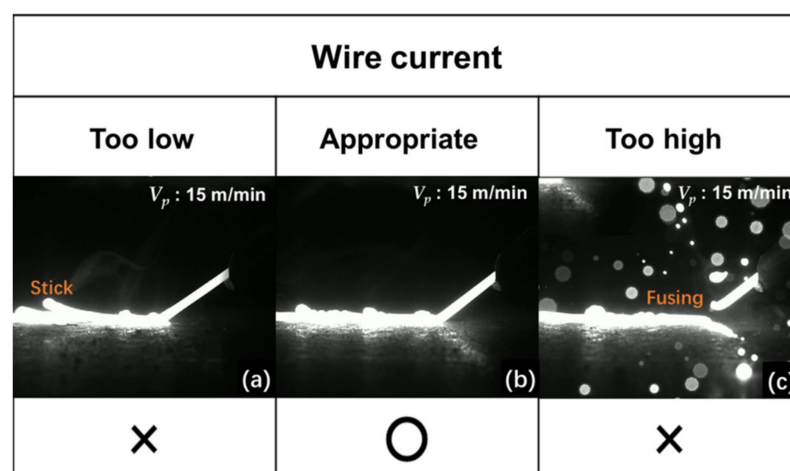


Figure 13. Three types of hot-wire heating phenomena: (a) stick, (b) smooth, and (c) fusing.

The same tendency was confirmed for all hot-wire feeding speeds from 5 to 20 m/min. The estimates and experimental investigations showed that the wire tip temperature must

be near its melting point to achieve smooth and stable hot-wire feeding with a high feeding speed by setting the appropriate wire current. Efficient hot-wire feeding can be achieved on many filler wire types by setting the appropriate wire current that was estimated by using the proposed calculation method based on each material property.

4.2. Melting Phenomena during Three-Layer Deposition

Figure 14 shows high-speed images during processing for various combinations of process speed and laser power using a fixed wire feeding rate of 20. Figure 14a shows that when the process speed (V_p) was 0.3 m/min and the laser power (P) was 4 kW for a fixed wire feeding rate (WFR) of 20, the filler wire was fed smoothly and continuously at the centers of the laser beam spot and molten pool front in the width direction during deposition. The same wire feeding and melting phenomena were observed at higher process speeds of 0.4 and 0.5 m/min when a higher laser power from 4.4 to 5.5 kW was applied, as shown in Figure 14c. These smooth and stable melting phenomena yielded smooth and sound bead appearances. When a higher process speed of 0.4 m/min was applied for a fixed laser power of 4 kW, the filler wire was not fed smoothly and stably into the molten pool, and it protruded from the molten pool as shown in Figure 14b. The same tendency was observed at other process speeds of 0.3 and 0.5 m/min when a laser power of 3 and 5 kW was applied, respectively, as shown in Figure 14d. Low-quality three-layer deposition with unmelted protruded wires at the bead sides was observed, as shown in Figure 14b,d.

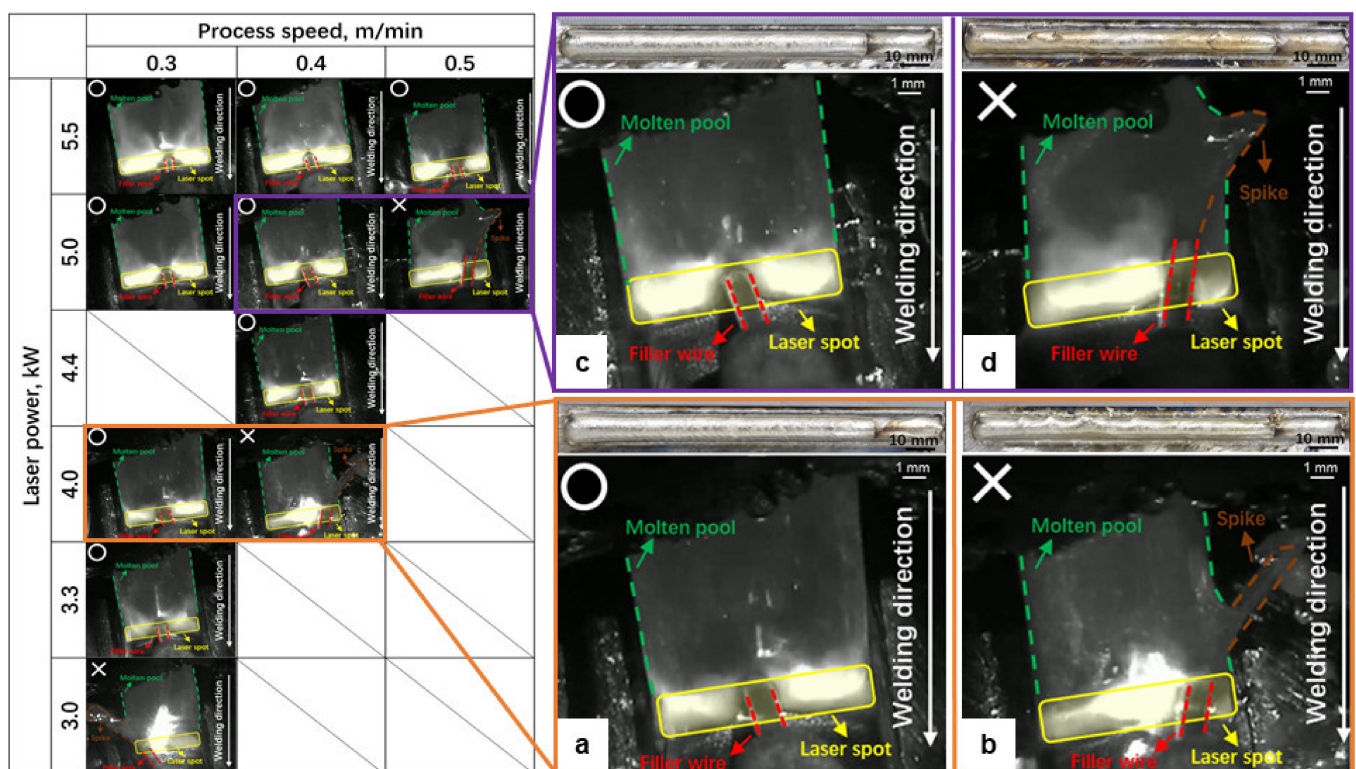


Figure 14. High-speed images during processing for various combinations of process speed and laser power using fixed wire feeding rate of 20 m/min: (a) $P = 4.0$ kW, $V_p = 0.3$ m/min, (b) $P = 4.0$ kW, $V_p = 0.4$ m/min, (c) $P = 5.0$ kW, $V_p = 0.4$ m/min, and (d) $P = 5.0$ kW, $V_p = 0.5$ m/min.

Figure 15 shows high-speed images during processing for various combinations of wire feeding rates and laser power using a fixed process speed of 0.3 m/min. Figure 15a shows that when the WFR is 30 and the laser power (P) is 5 kW at a fixed process speed of 0.3 m/min, the filler wire is fed smoothly and continuously at the center of the laser beam spot and molten pool front in the width direction during deposition. The same smooth and

stable processing phenomena were observed at other wire feeding rates of 20 and 40 with appropriate laser powers, as shown in Figure 15a. When a larger wire feeding rate of 40 was used at a fixed laser power of 5 kW, the filler wire was not fed smoothly and stably into the molten pool, and it protruded from the molten pool, as shown in Figure 15d. The same tendency was observed at other wire feeding rates of 20 and 30 m/min when a lower laser power was applied, as shown in Figure 15b. Almost the same processing phenomena and bead creations were observed for both combinations of laser power and process speed for a fixed wire feeding speed and laser power and wire feeding rate at a fixed process speed.

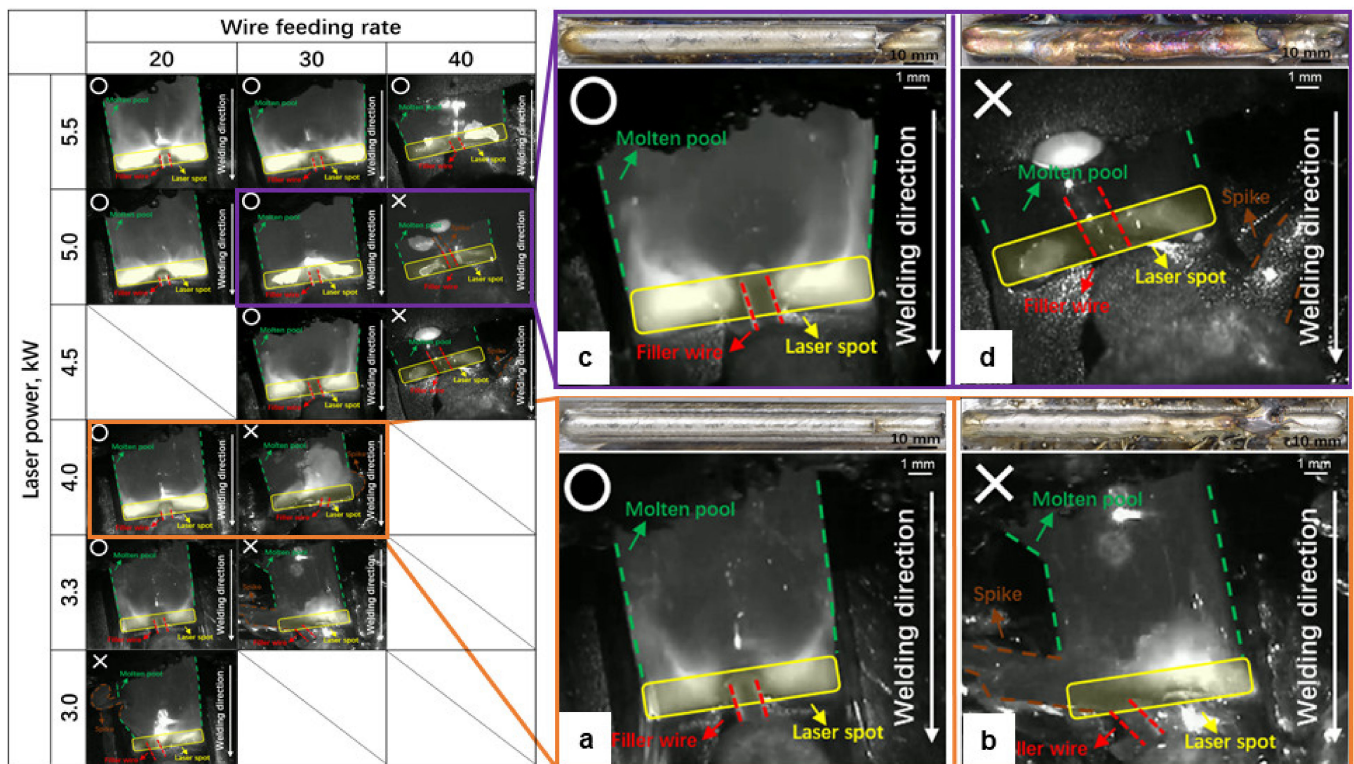


Figure 15. High-speed images during processing for various combinations of wire feeding rate and laser power using fixed process speed of 0.3 m/min: (a) $P = 3.3$ kW, WFR = 20, (b) $P = 3.3$ kW, WFR = 30, (c) $P = 4.5$ kW, WFR = 30, and (d) $P = 4.5$ kW, WFR = 40.

Figure 16 shows the evaluated results of the deposited three-layer appearance quality on the relationship between the energy heat input (see Equation (8)) and the wire feeding rate. When the wire feeding rate was 20, a sound bead was obtained for an energy heat input above ~ 35 J/mm³. The energy heat input of 35 J/mm³ as the limitation of the lowest energy heat input to achieve the sound bead was constant even if the process speed was varied from 0.3 to 0.5 m/min. When the wire feeding rate increased to 30 and 40, limitations of the lowest energy heat input of ~ 48 J/mm³ and 60 J/mm³ resulted to achieve a sound bead, respectively.

The above results confirm that the energy heat input is a key factor to achieve appropriate processing phenomena with a stable and sufficient wire melting and molten pool formation. A low energy heat input, a higher process speed, or a lower laser power makes it difficult to melt the filler wire stably and smoothly as well as to melt the substrate surface or formerly deposited layer surface. Therefore, wire sticking occurs, and a low-quality deposited bead forms. A higher energy heat input is required when the wire feeding rate increases. A larger material volume with a temperature immediately below its melting point from hot-wire feeding needs a higher heat input to melt the material perfectly. A larger volume of molten pool interferes with the heat input into the substrate or formerly

deposited bead surface, and unstable and insufficient molten pool formation occurs during the subsequent bead deposition.

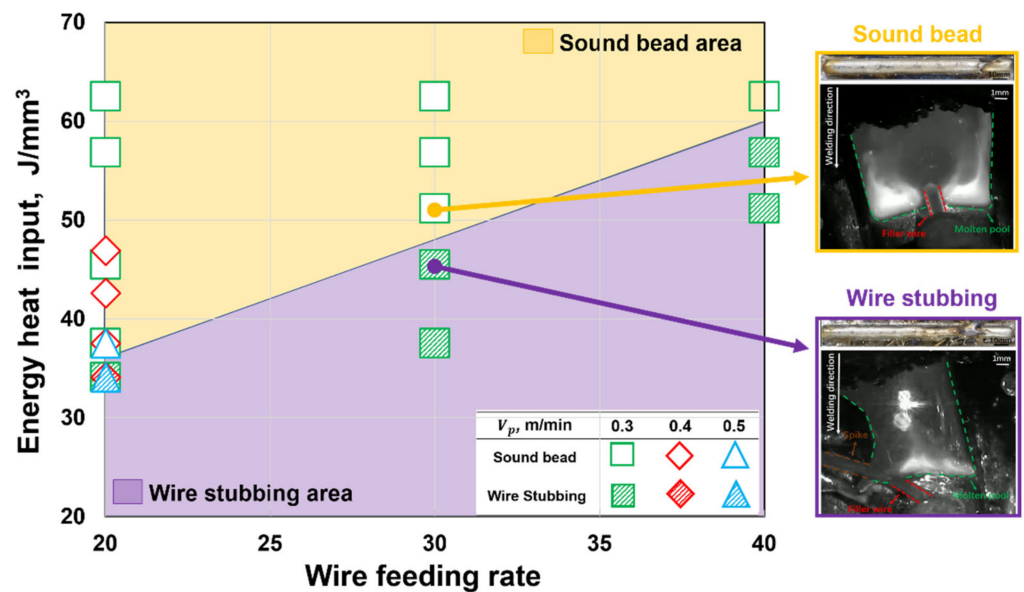


Figure 16. Appearance quality of deposited three layers.

4.3. Effect of Process Parameters on Cross-Sectional Characteristics

The effect of the process parameters of laser power, process speed, and the wire feeding rate on the cross-sectional characteristics (e.g., effective width, effective height, maximum height, and the near net shape rate) was investigated. Figure 17 shows the bead appearances and cross-sections when the laser power varied from 3.3 to 5.5 kW, and two types of wire feeding rates of 20 and 30 were used at a fixed process speed of 0.3 m/min. Although the laser power was varied extensively, and the wire feeding rate changed with a 1.5 time, smooth and stable bead appearances, and sound cross-sections without any defects resulted on all deposited samples. A smaller wire feeding rate of 20 resulted in a narrower bead with increased layers, and a larger laser power resulted in a wider bead with an increase in layers for a larger wire feeding rate of 30.

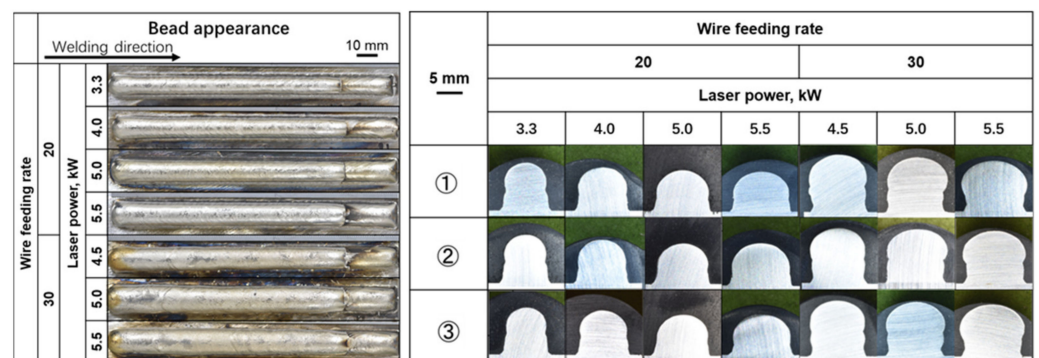


Figure 17. Bead appearances and cross-sections ($V_p = 0.3$ m/min).

Figure 18 shows the effective width, the effective height and maximum height, and the near net shape rate measured on the cross-sections in Figure 17. The effective width (see Figure 18a) increased almost linearly with an increase in laser power for wire feeding speeds of 20 and 30. Figure 17 shows that the higher laser power yielded a wider substrate surface melting width and maintained a wider width on the third layer. The effect of wire feeding speeds of 20 and 30 was small compared with the effect of laser power on the effective width. The effective height and maximum height (see Figure 18b) decreased

almost linearly with an increase in laser power for wire feeding speeds of 20 and 30. Figure 17 shows that an increase in width resulted in a decrease in height for a fixed wire feeding speed. The effect of wire feeding speeds of 20 and 30 was large compared with the effect of laser power at both heights. The near net shape rate (see Figure 18c) decreased with an increase in laser power, and it increased at the high laser power condition of 5.5 kW for both wire feeding speeds of 20 and 30. The effect of wire feeding speeds of 20 and 30 was large compared with the effect of laser power on the near net shape rate. The combination of a 5.5-kW laser power and a wire feeding rate of 30 for the fixed 0.3 m/min process speed achieved an effective width above 10 mm, an effective height above 7 mm, and a near net shape rate of over 75%.

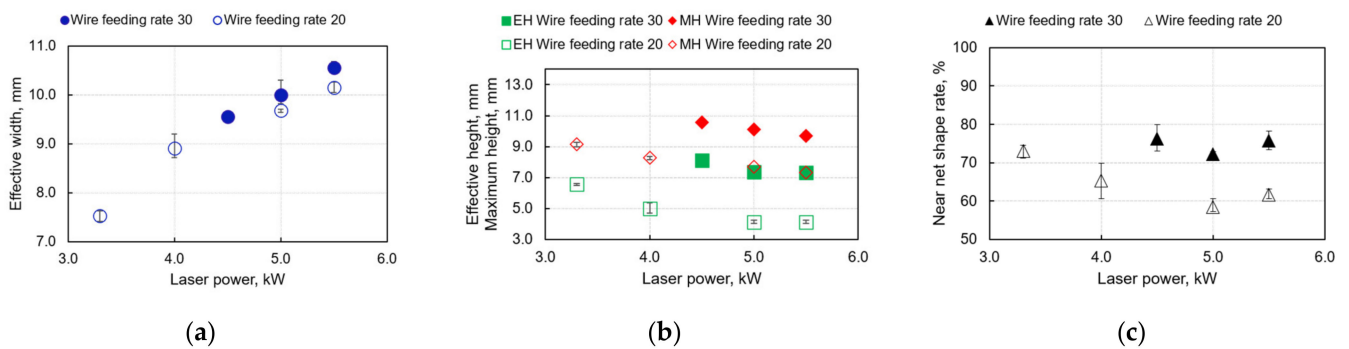


Figure 18. Cross-sectional characteristics ($V_p = 0.3$ m/min): (a) effective width, (b) effective height and maximum height, and (c) near net shape rate.

Figure 19 shows the bead appearances and cross-sections for a varied process speed from 0.24 to 0.5 m/min, and two types of wire feeding rates of 20 and 30 at a fixed laser power of 5.5 kW. Although the process speed varied extensively and the wire feeding rate also changed, a smooth and stable bead appearance and sound cross-sections without any defects were visible on all deposited samples. For the 20 wire feeding rates, a smaller height formed under the lower-speed condition, and a narrower width resulted for the larger speed condition. The difference in bead shape on the wire feeding rate of 30 was smaller than for the wire feeding rate of 20.

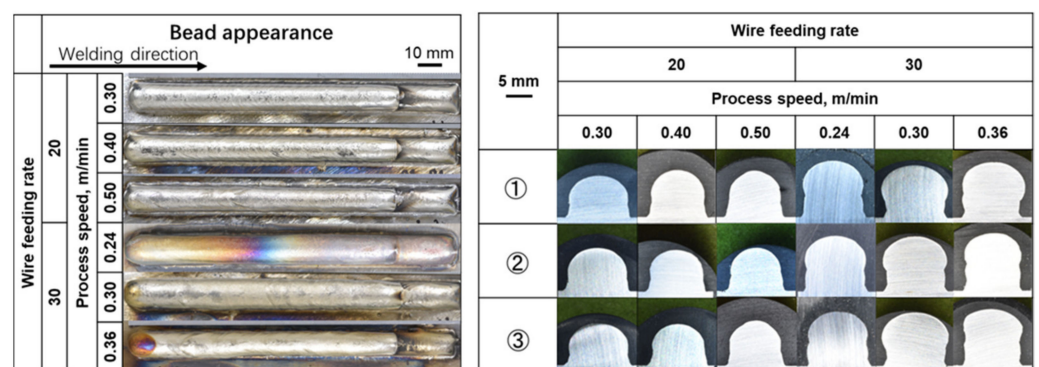


Figure 19. Bead appearances and cross-sections ($P = 5.5$ kW).

Figure 20 shows the effective width, the effective height and maximum height, and the near net shape rate measured on the cross-sections in Figure 19. The effective width (see Figure 20a) decreased almost linearly with the increase in process speed for both wire feeding speeds of 20 and 30 because the higher process speed decreased the heat input and melting width of the substrate surface. However, the effective width was saturated at ~10.5 mm in the slower process speed region because the laser beam spot with an 11-mm width was used in this study. The effect of wire feeding speeds of 20 and 30 was small compared with the effect of process speed on the effective width. The effective height and

maximum height (see Figure 20b) increased gradually with the increase in process speed for both wire feeding speeds of 20 and 30 because the width decreased for the fixed wire feeding speed. Height saturation occurred in the slower process speed region for both wire feeding speeds of 20 and 30 as occurred for the effective bead width. The effect of wire feeding speeds of 20 and 30 was large compared with the effect of process speed on both heights. The near net shape rate (see Figure 20c) increased with an increase in process speed for both wire feeding speeds of 20 and 30. The effect of wire feeding speeds of 20 and 30 was large compared with the effect of process speed on the near net shape rate. The combination of a 0.36 m/min process speed and a 30-wire feeding rate for a fixed 5.5-kW laser power achieved an effective width above 10 mm, an effective height of ~8 mm, and a near net shape rate above 75%.

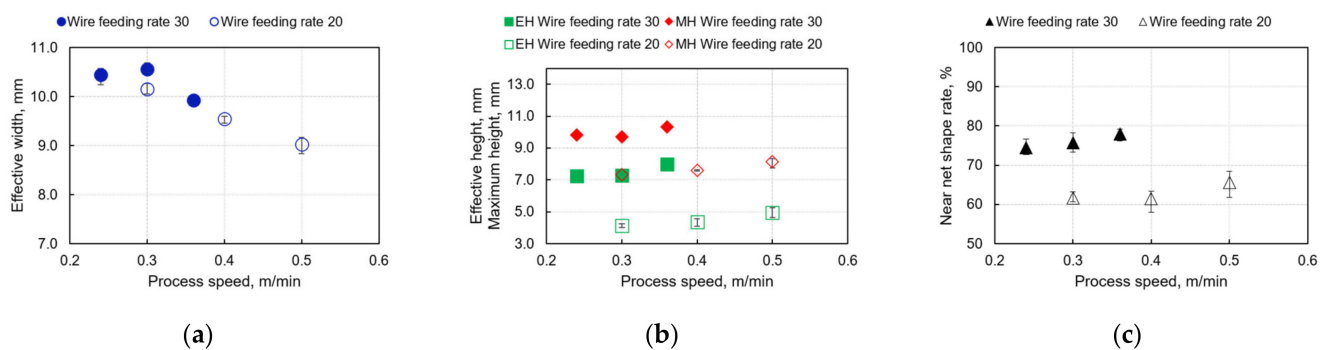


Figure 20. Cross-sectional characteristics ($P = 5.5$ kW): (a) effective width, (b) effective height and maximum height, and (c) near net shape rate.

5. Conclusions

A simple calculation method was proposed to derive an appropriate hot-wire current for Z3321-YS308L. The method was evaluated by hot-wire feeding experiments using high-speed imaging. Process windows to obtain sound beads for various combinations of process parameters were obtained by three-layer deposition. The effect of process parameters on processing phenomena, the bead appearance, and the cross-sectional characteristics was discussed in detail by using high-speed images and cross-sectional measurements. The conclusions were as follows:

1. The wire current has a critical effect on wire melting and feeding phenomena, and a current that is too low or too high results in sticking or fusing and spattering, respectively. The estimated appropriate wire current from the proposed method agreed well with the experimental result for a wide range of wire feeding speeds from 0 to 20 m/min.
2. Process windows for a laser power from 3 to 5.5 kW, process speeds from 0.3 to 0.5, and a wire feeding rate from 20 to 40 were obtained. A high efficiency with almost 100% material utilization and a high deposition rate above 800 cm³/h were achieved.
3. A 15-layer wall-type sample of 50 mm in height, 8 mm in width, and 250 mm in length was fabricated by using the optimized conditions, and tensile tests were performed by using a specimen that was cut from the wall-type sample. A sound large sample with an 83% near net shape rate without any defects and a sufficient strength (558 MPa) and elongation (49%) were achieved.
4. The energy heat input was proposed as being key to obtaining adequate and stable melting phenomena. Each wire feeding rate from 20 to 40 had a lower limitation of energy heat input from 35 to 60 J/mm³ to create sound deposited layers.
5. The laser power and process speed affected the effective width and effective height and maximum height, respectively. The wire feeding rate had the biggest effect on height and the near net shape rate. A sufficiently high wire feeding speed (rate) should be used according to the laser beam width and processing speed before optimizing other parameters in the proposed HLAM process.

Author Contributions: Conceptualization, S.Z. and M.Y.; methodology, S.Z. and M.Y.; investigation, S.Z. and Y.N.; data curation, S.Z.; writing-original draft preparation, S.Z.; writing-review and editing, S.Z. and M.Y.; supervision, M.Y. All authors have read and agreed to the published version of the manuscript.

Funding: This research received no external funding.

Data Availability Statement: Not applicable.

Conflicts of Interest: The authors declare no conflict of interest.

References

1. DebRoy, T.; Wei, H.L.; Zuback, J.S.; Mukherjee, T.; Elmer, J.W.; Milewski, J.O.; Beese, A.M.; Wilson-Heid, A.; De, A.; Zhang, W. Additive manufacturing of metallic components—Process, structure and properties. *Prog. Mater. Sci.* **2018**, *92*, 112–224. [[CrossRef](#)]
2. Milewski, J.O. *Additive Manufacturing of Metals*; Springer Series in Materials Science; Springer: Berlin/Heidelberg, Germany, 2017; Volume 258, pp. 7–33.
3. Cawley, J.D. Solid freeform fabrication of ceramics. *Curr. Opin. Solid State Mater. Sci.* **1999**, *4*, 483–489. [[CrossRef](#)]
4. Sandeep, D.C. Comparison and analysis of different 3D printing techniques. *Int. J. Eng. Technol.* **2017**, *8*, 264–272.
5. Syed, A.M.T.; Elias, P.K.; Amit, B.; Susmita, B.; Lisa, O.; Costas, C. Additive manufacturing: Scientific and technological challenges, market uptake and opportunities. *Mater. Today* **2018**, *21*, 22–37.
6. Frazier, W.E. Metal Additive Manufacturing: A Review. *J. Mater. Eng. Perform.* **2014**, *23*, 1917–1928. [[CrossRef](#)]
7. Schultz, V.; Seefeld, T.; Vollertsen, F. Gap bridging ability in laser beam welding of thin aluminum sheets. *Phys. Procedia* **2014**, *56*, 545–553. [[CrossRef](#)]
8. Singh, R.; Gupta, A.; Tripathi, O.; Srivastava, S.; Singh, B.; Awasthi, A.; Rajput, S.K.; Sonia, P.; Singhal, P.; Saxena, K.K. Powder bed fusion process in additive manufacturing: An overview. *Mater. Today* **2020**, *26*, 3058–3070. [[CrossRef](#)]
9. Bandyopadhyay, A.; Bose, S. *Additive Manufacturing*, 1st ed.; CRC Press: Boca Raton, FL, USA, 2015; pp. 2–24.
10. Gibson, I.; Rosen, D.W.; Stucker, B. *Additive Manufacturing Technologies: 3D Printing, Rapid Prototyping, and Direct Digital Manufacturing*; Springer: New York, NY, USA, 2009; pp. 4–38.
11. Oliveira, J.P.; Santos, T.G.; Miranda, R.M. Revisiting fundamental welding concepts to improve additive manufacturing: From theory to practice. *Prog. Mater. Sci.* **2020**, *107*, 100590. [[CrossRef](#)]
12. Oliveira, J.P.; LaLonde, A.D.; Ma, J. Processing parameters in laser powder bed fusion metal additive manufacturing. *Mater. Des.* **2020**, *193*, 108762. [[CrossRef](#)]
13. Joshi, S.C.; Sheikh, A.A. 3D printing in aerospace and its long-term sustainability. *Virtual. Phys. Prototyp.* **2015**, *10*, 175–185. [[CrossRef](#)]
14. Nie, Z.G.; Wang, G.; McGuffin-Cawley, J.D.; Narayanan, B.; Zhang, S.J.; Schwam, D.; Kottman, M.; Rong, Y.M. Experimental study and modeling of H13 steel deposition using laser hot-wire additive manufacturing. *J. Mater. Process. Technol.* **2016**, *235*, 171–186. [[CrossRef](#)]
15. Tang, S.Y.; Wang, G.L.; Song, H.; Li, R.S.; Zhang, H.O. A novel method of bead modeling and control for wire and arc additive manufacturing. *Rapid Prototyp. J.* **2021**, *27*, 311–320. [[CrossRef](#)]
16. Fang, X.; Ren, C.; Zhang, L.; Wang, C.; Huang, K.; Lu, B. A model of bead size based on the dynamic response of CMT-based wire and arc additive manufacturing process parameters. *Rapid Prototyp. J.* **2021**, *27*, 741–753. [[CrossRef](#)]
17. Dai, F.; Zhang, H.; Li, R. Process planning based on cylindrical or conical surfaces for five-axis wire and arc additive manufacturing. *Rapid Prototyp. J.* **2020**, *26*, 1405–1420. [[CrossRef](#)]
18. Kulkarni, J.D.; Goka, S.B.; Parchuri, P.K.; Yamamoto, H.; Ito, K.; Simhambhatla, S. Microstructure evolution along build direction for thin-wall components fabricated with wire-direct energy deposition. *Rapid Prototyp. J.* **2021**, *27*, 1289–1301. [[CrossRef](#)]
19. Rodrigues, T.A.; Duarte, V.R.; Miranda, R.M.; Santos, T.G.; Oliveira, J.P. Ultracold-Wire and arc additive manufacturing (UC-WAAM). *J. Mater. Process. Technol.* **2021**, *296*, 117196. [[CrossRef](#)]
20. Li, Z.X.; Liu, C.M.; Xu, T.Q.; Ji, L.; Wang, D.H.; Lu, J.P.; Ma, S.Y.; Fan, H.L. Reducing arc heat input and obtaining equiaxed grains by hot-wire method during arc additive manufacturing titanium alloy. *J. Mater. Sci. Eng. A* **2019**, *742*, 287–294. [[CrossRef](#)]
21. Yan, W.Z.; Yue, Z.F.; Zhang, J.Z. Study on the residual stress and warping of stiffened panel produced by electron beam freeform fabrication. *Mater. Des.* **2016**, *89*, 1205–1212. [[CrossRef](#)]
22. Chang, S.H.; Gach, S.; Senger, A.; Zhang, H.Y.; Du, D. A new 3D printing method based on non-vacuum electron beam technology. *J. Phys. Conf. Ser.* **2018**, *1074*, 012017. [[CrossRef](#)]
23. Chlebus, E.; Gruber, K.; Kuźnicka, B.; Kurzac, J.; Kurzynowski, T. Effect of heat treatment on the microstructure and mechanical properties of Inconel 718 processed by selective laser melting. *Mater. Sci. Eng. A* **2015**, *639*, 647–655. [[CrossRef](#)]
24. Criales, L.E.; Arisoy, Y.M.; Lane, B.; Moylan, S.; Donmez, A.; Ozel, T. Laser powder bed fusion of nickel alloy 625: Experimental investigations of effects of process parameters on melt pool size and shape with spatter analysis. *Int. J. Mach. Tools Manuf.* **2017**, *121*, 22–36. [[CrossRef](#)]
25. Jadhav, S.D.; Dhekne, P.P.; Brodu, E.; Hooreweder, B.V.; Dadbakhsh, S.; Kruth, J.P.; Humbeek, J.V.; Vanmeensel, K. Laser powder bed fusion additive manufacturing of highly conductive parts made of optically absorptive carburized CuCr1 powder. *Mater. Des.* **2021**, *198*, 109369. [[CrossRef](#)]

26. Ma, M.M.; Wang, Z.M.; Wang, D.Z.; Zeng, X.Y. Control of shape and performance for direct laser fabrication of precision large-scale metal parts with 316L Stainless Steel. *Opt. Laser Technol.* **2013**, *45*, 209–216. [[CrossRef](#)]
27. Shaikh, M.O.; Chen, C.-C.; Chiang, H.-C.; Chen, J.-R.; Chou, Y.-C.; Kuo, T.-Y.; Ameyama, K.; Chuang, C.-H. Additive manufacturing using fine wire-based laser metal deposition. *Rapid Prototyp. J.* **2020**, *26*, 473–483. [[CrossRef](#)]
28. Yang, D.X.; Li, X.Y.; He, D.Y.; Nie, Z.R.; Huang, H. Optimization of weld bead geometry in laser welding with filler wire process using Taguchi's approach. *Opt. Laser Technol.* **2012**, *44*, 2020–2025.
29. Du, F.R.; Zhu, J.Q.; Ding, X.P.; Zhang, Q.; Ma, H.L.; Yang, J.; Cao, H.Z.; Ling, Z.M.; Wang, G.Y.; Duan, X.M.; et al. Dimensional characteristics of Ti-6Al-4V thin-walled parts prepared by wire-based multi-laser additive manufacturing in vacuum. *Rapid Prototyp. J.* **2019**, *25*, 849–856. [[CrossRef](#)]
30. Yamamoto, M.; Shinozaki, K.; Kadoi, K.; Fujita, D.; Inoue, T.; Fukahori, M.; Kitahara, Y. Development of hot-wire laser welding method for lap joint of steel sheet with wide gap. *Q. J. Jpn. Weld. Soc.* **2011**, *29*, 58–61. [[CrossRef](#)]
31. Kadoi, K.; Shinozaki, K.; Yamamoto, M.; Owaki, K.; Inose, K.; Takayanagi, D. Development of high-efficiency/high-quality hot-wire laser fillet welding process. *Q. J. Jpn. Weld. Soc.* **2011**, *29*, 62–65. [[CrossRef](#)]
32. Wen, P.; Cai, Z.P.; Feng, Z.H.; Wang, G. Microstructure and mechanical properties of hot wire laser clad layers for repairing precipitation hardening martensitic stainless steel. *Opt. Laser Technol.* **2015**, *75*, 207–213. [[CrossRef](#)]
33. Shinozaki, K.; Yamamoto, M.; Nagamitsu, Y.; Uchida, T.; Mitsuhata, K.; Nagashima, T.; Kanazawa, T.; Arashin, H. Melting phenomenon during ultra-high-speed GTA welding method using pulse-heated hot-wire. *Q. J. Jpn. Weld. Soc.* **2009**, *27*, 22–26. [[CrossRef](#)]
34. Liu, W.; Liu, S.; Ma, J.J.; Kovacevic, R. Real-time monitoring of the laser hot-wire welding process. *Opt. Laser Technol.* **2014**, *57*, 66–76. [[CrossRef](#)]
35. Nurminen, J.; Riihimäki, J.; Näkki, J.; Vuoristo, P. Comparison of laser cladding with powder and hot and cold wire techniques. *J. Laser Appl.* **2006**, *1006*. [[CrossRef](#)]
36. Wei, H.Y.; Zhang, Y.; Tan, L.P.; Zhong, Z.H. Energy efficiency evaluation of hot-wire laser welding based on process characteristic and power consumption. *J. Clean. Prod.* **2015**, *87*, 255–262. [[CrossRef](#)]
37. Charunetratsamee, S.; Warinsiriruk, E.; Shinozaki, K.; Yamamoto, M. Melting by Reflected Laser Beam during Vertical Welding via Hot-Wire Laser Welding. *Q. J. Jpn. Weld. Soc.* **2019**, *37*, 208–214.
38. Takaya, S.; Yamamoto, M.; Shinozaki, K.; Matsuda, H.; Ikeda, R. Hot-wire Laser Brazing Technology for Steel/Aluminum Alloy Dissimilar Joint. *Q. J. Jpn. Weld. Soc.* **2017**, *35*, 155–159. [[CrossRef](#)]
39. Todo, M.; Shinozaki, K.; Yamamoto, M.; Kadoi, K.; Yamamoto, M.; Phaonaim, R.; Okagaito, T. Hot-wire Laser Welding Process Using Laser Diode for Large-Diameter Pipe with Narrow Gap Joint. *Q. J. Jpn. Weld. Soc.* **2017**, *35*, 107–110. [[CrossRef](#)]
40. Xiao, M.; Gao, C.K.; Tan, C.W.; Zhao, Y.X.; Liu, H.B.; Yang, J. Experimental and numerical assessment of interfacial microstructure evolution in dissimilar Al/steel joint by diode laser welding-brazing. *Optik* **2021**, *245*, 167706. [[CrossRef](#)]